

# Energy Advances

Accepted Manuscript

This article can be cited before page numbers have been issued, to do this please use: I. Madakannu, A. Shankar, G. Maduraiveeran and K. K. R. Datta, *Energy Adv.*, 2026, DOI: 10.1039/D6YA00052E.



This is an Accepted Manuscript, which has been through the Royal Society of Chemistry peer review process and has been accepted for publication.

Accepted Manuscripts are published online shortly after acceptance, before technical editing, formatting and proof reading. Using this free service, authors can make their results available to the community, in citable form, before we publish the edited article. We will replace this Accepted Manuscript with the edited and formatted Advance Article as soon as it is available.

You can find more information about Accepted Manuscripts in the [Information for Authors](#).

Please note that technical editing may introduce minor changes to the text and/or graphics, which may alter content. The journal's standard [Terms & Conditions](#) and the [Ethical guidelines](#) still apply. In no event shall the Royal Society of Chemistry be held responsible for any errors or omissions in this Accepted Manuscript or any consequences arising from the use of any information it contains.

# Tailoring $\text{MMn}_2\text{O}_4$ Spinels Anchored on Nitrogen doped Reduced Graphene Oxide for High Performance Bifunctional Water Splitting

Madakannu Iyyappan,<sup>a</sup> Ayyavu Shankar,<sup>a</sup> Govindan Maduraiveeran<sup>\*a,b</sup> and K. K. R. Datta<sup>\*a</sup>

<sup>a</sup>Department of Chemistry, Faculty of Engineering and Technology, SRM Institute of Science and Technology, Kattankulathur – 603203, Tamil Nadu, India.

<sup>b</sup>Materials Research Center, American University of Sharjah, Sharjah, 26666, United Arab Emirates

*\*Corresponding Author:* mgovindhan@aus.edu & pgmadura@yahoo.co.in (GM) and kumarard@srmist.edu.in & kkrdatta@gmail.com (KKRD)

## ABSTRACT

Developing highly efficient, durable, and low-cost oxygen evolution reaction (OER) electrode remains a key barrier that needs to be overcome for producing green  $\text{H}_2$  through alkaline water electrolysis (AWE). A series of transition metal cation-substituted manganese oxides ( $\text{M-Mn}_2\text{O}_4$ , where  $\text{M} = \text{Co}, \text{Cu}, \text{Fe}, \text{and Zn}$ ) over nitrogen-doped rGO (N-rGO) nanosheet ( $\text{M-Mn}_2\text{O}_4@\text{N-rGO}$ ) heterostructures using a facile solvothermal strategy were developed. Among the tested compositions, the  $\text{FeMn}_2\text{O}_4@\text{N-rGO}$  heterostructures exhibited superior OER catalytic activity, with an overpotential ( $\eta$ ) of  $\sim 330$  mV at  $10 \text{ mA cm}^{-2}$  along with stability over 96 h in 1 M KOH. In addition to OER activity, the  $\text{FeMn}_2\text{O}_4@\text{N-rGO}$  heterostructure exhibited better hydrogen evolution reaction (HER) performance, achieving an overpotential of 153 mV at a current density  $10 \text{ mA cm}^{-2}$ . The coexistence of  $\text{Fe}^{3+}/\text{Fe}^{2+}$  and  $\text{Mn}^{3+}/\text{Mn}^{4+}$  redox couples provide multiple electron transfer pathways during water splitting. When assembled as a bifunctional electrode for overall water splitting ( $\text{FeMn}_2\text{O}_4@\text{N-rGO}$  as both anode and cathode), the system delivers a cell voltage of 1.57 V at  $10 \text{ mA cm}^{-2}$ , with operational stability over 10 h. The robust spinel framework, strong metal–support interactions confirm that  $\text{FeMn}_2\text{O}_4@\text{N-rGO}$  is a viable electrocatalyst for AWE systems

**Keywords:** Manganese spinel oxides, Metal cation substitution, Nitrogen-doped reduced graphene oxide, Solvothermal synthesis, Water Splitting

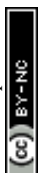


## Introduction

View Article Online  
DOI: 10.1039/D6YA00052E

Alkaline water electrolyzer (AWE) has gained extensive attention in recent years due to the pressing global energy crisis and the growing demand for sustainable hydrogen generation technologies. Among the available methods, water electrolysis has emerged as a promising strategy for producing green hydrogen with high purity, holding immense potential for decarbonizing the energy sector.<sup>[1-3]</sup> This process involves two key half-cell reactions: the oxygen evolution reaction (OER) and the hydrogen evolution reaction (HER).<sup>[4]</sup> In particular, OER remains a bottleneck due to its high overpotential and slow kinetics, which directly impact the overall efficiency of energy conversion systems. Consequently, considerable research efforts have been directed toward developing highly efficient OER electrocatalysts to overcome these challenges, specifically aiming to reduce overpotential and accelerate reaction kinetics through two-electron or four-electron pathways. Precious metal oxides, such as RuO<sub>2</sub> and IrO<sub>2</sub>, have demonstrated excellent OER activity in both acidic and alkaline media.<sup>[5, 6]</sup> However, their widespread adoption is limited due to their susceptibility to oxidation under high anodic potentials, high cost, and stability issues during prolonged operation.

On the other hand, metal complexes, transition-metal-based catalysts include oxides, sulphides, phosphides of Fe, Ni, Co, Cu, Zn, Mn, MOF-derived composites, besides single-atom catalysts have shown promise in catalytic activity as earth-abundant alternatives.<sup>[7-14]</sup> The stability and performance of these catalysts are strongly influenced by the pH of the electrolyte; generally, alkaline media are often preferred for stability due to the variable oxidation states of transition metals. Among transition-metal oxides, spinel oxides have garnered significant attention for OER due to their tunability, cost-effectiveness, simple synthesis, compositional diversity, and stability in alkaline solutions.<sup>[15, 16]</sup> Spinel-structured materials can be classified as monometallic (Co<sub>3</sub>O<sub>4</sub>, Mn<sub>3</sub>O<sub>4</sub>, Fe<sub>3</sub>O<sub>4</sub>, and more) or bimetallic (NiCo<sub>2</sub>O<sub>4</sub>, CoMn<sub>2</sub>O<sub>4</sub>, CoFe<sub>2</sub>O<sub>4</sub>, etc.) based on the transition metals occupying the A and B sites.<sup>[17, 18]</sup> Inverse spinel



structure possessing  $(A^{2+}_{oh})(B^{3+}_{tet})(B^{3+}_{oh})O_4$ , features A-site cations in octahedral sites and B-site cations distributed between tetrahedral and octahedral sites. This structural flexibility facilitates tailored modifications, a necessary attribute toward enhanced electrocatalytic activity. Recently, several inverse spinel-based binary and ternary metal oxides have been used in OER applications, including  $NiFe_2O_4$ <sup>[19]</sup>,  $NiCo_2O_4$ <sup>[20, 21]</sup>,  $MnCo_2O_4$ <sup>[22]</sup>,  $NiMn_2O_4$ <sup>[23]</sup>,  $Co_{1-x}Ni_xFe_2O_4$ <sup>[24]</sup>, and more.

Manganese-based inverse spinel is particularly notable for its multivalent nature, with Mn ions existing in oxidation states such as  $Mn^{2+}$ ,  $Mn^{3+}$ ,  $Mn^{4+}$ ,  $Mn^{6+}$ , and  $Mn^{7+}$ .<sup>[25-27]</sup> This versatility provides diverse binding sites (M-OH, M-OOH, and M-O) that are crucial for the OER under anodic polarization in alkaline solutions.<sup>[28, 29]</sup> In alkaline media, Mn-based materials are prone to disproportionation reactions at +3 and +6 oxidation states. Specifically,  $Mn^{3+}$  species disproportionate into  $Mn^{2+}$  and  $Mn^{4+}$  to  $MnO_2$ , while  $Mn^{2+}$  dissolves into the electrolyte. Similarly,  $Mn^{6+}$  species formed during graphene oxide (GO) synthesis form a stable  $MnO_2$  and  $Mn^{7+}$  species, which dissociate as  $MnO_4^-$  ions from the electrode surface.<sup>[27]</sup> Over time, this process leads to a gradual transformation of the initial electrode material into  $MnO_2$ . Eventually, the  $MnO_x$  structure degrades during OER, forming permanganate species, losing active material to the electrolyte, which hinders their long-term catalytic performance. These challenges highlight the need for structural and compositional modifications to stabilize Mn-based spinel toward improved electrocatalytic performance.

To address these shortcomings, researchers have explored compositional modifications and supportive frameworks, such as nickel foam (NF),<sup>[30]</sup> graphene, reduced graphene oxide (rGO),<sup>[31-33]</sup> and carbon nanotubes (CNTs)<sup>[34, 35]</sup> to enhance dispersion, conductivity, and durability of the spinel.<sup>[36]</sup> Additionally, heteroatom doping has emerged as a powerful strategy to modulate the electronic structure and active sites of electrocatalysts. Among various dopants, nitrogen stands out due to its ability to create electron-rich regions and improve charge transfer



efficiency, thereby boosting catalytic performance.<sup>[37]</sup> These combined approaches significantly advance the design of robust and efficient electrocatalysts. For instance, drop-casting Mn spinel supported by N-rGO onto nickel foam has demonstrated significant improvements in conductivity and interfacial electron transfer efficiency due to synergistic effects. The porous structure of nickel foam ensures high loading density and close contact between components, providing a high surface area for the uniform deposition of metal oxides. This reduces interfacial resistance and maximizes electron transport efficiency during OER. Additionally, its three-dimensional geometry promotes quick electrolyte penetration, ensuring effective ion transport and lowering charge transfer resistance, thereby improving the composite material's conductivity.<sup>[38]</sup>

Recent studies exemplify the potential of such Mn spinel's compositional modification. For instance, Gao et al. fabricated  $\text{FeMn}_2\text{O}_4$  via quenching and reported an overpotential of  $\sim 350$  mV at  $10 \text{ mA cm}^{-2}$ .<sup>[39]</sup> Peng et al. prepared Fe-doped  $\text{Mn}_3\text{O}_4$  ( $\text{Fe}_x\text{Mn}_{3-x}\text{O}_4$ ) on nickel foam, achieving an overpotential of  $\sim 258$  mV at  $20 \text{ mA cm}^{-2}$ . Gong et al. developed a multi-metal spinel catalyst ( $\text{Fe}_{12}\text{Ni}_{23}\text{Cr}_{10}\text{Co}_{30}\text{Mn}_{25}/\text{CNT}$ ), which demonstrated bifunctional activity with an overpotential of 0.7 V in 0.1 M KOH.<sup>[40]</sup> Furthermore, Wang et al. explored spinel oxide composites ( $\text{ACo}_2\text{O}_4/\text{NCNTs}$ , where A = Mn, Co, Ni, Cu, Zn) and highlighted the catalytic potential of  $\text{MnCo}_2\text{O}_4/\text{NCNTs}$  in oxygen reduction and evolution reactions.<sup>[41]</sup> Building upon these advancements, our study focuses on the development of a series of Mn-based spinels ( $\text{MMn}_2\text{O}_4$ , where M = Zn, Fe, Co, and Cu) embedded over nitrogen-doped rGO via a solvothermal-assisted method. Among the synthesized nanocomposites,  $\text{FeMn}_2\text{O}_4@\text{N-rGO}$  exhibited superior OER performance, demonstrating an overpotential of  $\sim 330$  mV at  $10 \text{ mA cm}^{-2}$  and considerable electrochemical durability, maintaining activity for 96 h in 1 M KOH with the cell voltage of 1.57 V. These findings underscore the potential of  $\text{FeMn}_2\text{O}_4@\text{N-rGO}$  as an efficient and durable electrocatalyst for OER and HER.



## Experimental

### Materials

All chemicals and solvents were used without further purification. Graphite flakes (20  $\mu\text{m}$ ), PVP ( $MW \approx 10000$ ) and  $\text{Fe}(\text{CH}_3\text{COO})_2 \cdot 4\text{H}_2\text{O}$  were purchased from Sigma Aldrich.  $\text{Zn}(\text{CH}_3\text{COO})_2 \cdot 2\text{H}_2\text{O}$ ,  $\text{Cu}(\text{CH}_3\text{COO})_2 \cdot 3\text{H}_2\text{O}$ ,  $\text{Mn}(\text{CH}_3\text{COO})_2 \cdot 4\text{H}_2\text{O}$  from SISCO SRL. ethanol was purchased from FISHER scientific.

### Synthesis of Graphite oxide (GO)

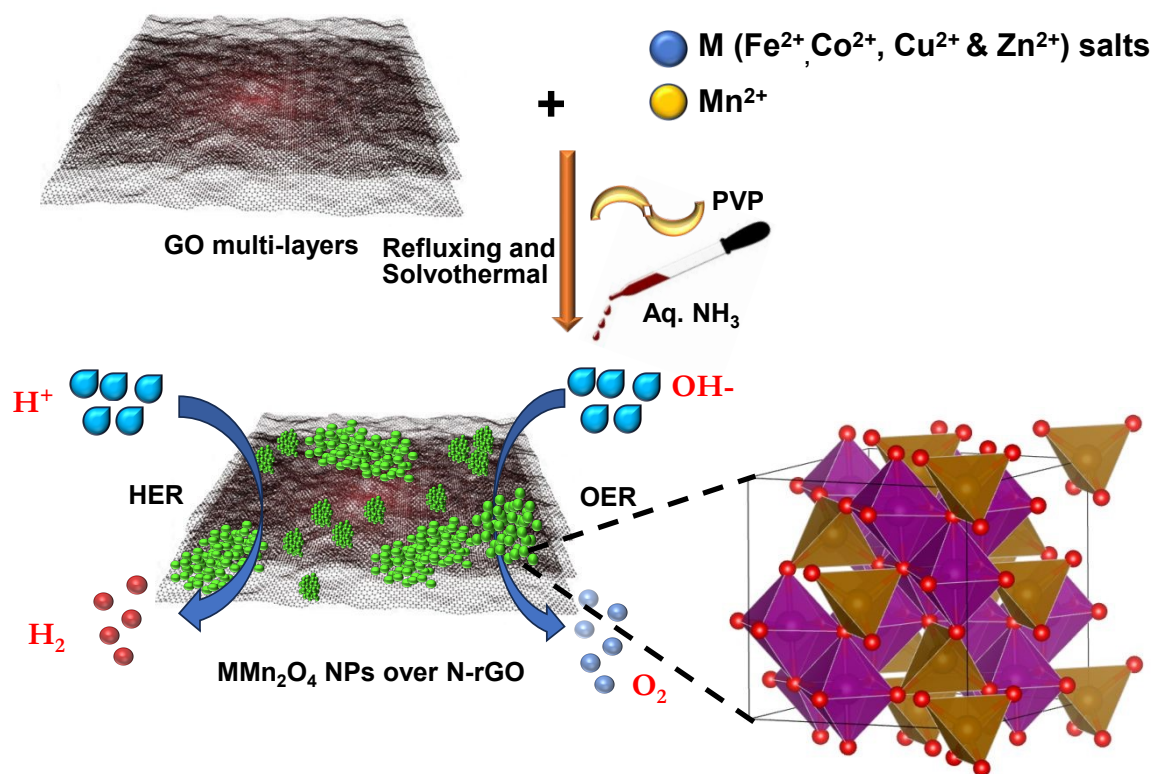
Graphite oxide was synthesized using a modified method described by Tour et al. and a procedure derived from our prior study<sup>[24]</sup>. Figure S1 shows the PXRD of synthesised graphene oxide.

### Preparation of Mn-based spinel oxides over N-doped reduced graphene (N- rGO)

0.4 mmol of metal acetate ( $M = \text{Zn}, \text{Co}, \text{Cu}, \text{and Fe}$ ) along with 0.8 mmol of manganese acetate were initially mixed in 50 mL of mixture of ethanol and water in a volume ratio of 19:1. To this solution, 0.6 mL of 25%  $\text{NH}_3$  solution, 0.07 g of PVP- M.Wt.10000 were added. To this, a separate solution of 0.1 g of GO was dispersed in 50 mL. The whole mixture was stirred magnetically at room temperature for 60 min. Subsequently, the solution was heated to reflux at 60  $^\circ\text{C}$  for a duration of 20 h. The resultant mixture was transferred to a 100 mL autoclave for a hydrothermal reaction at 120  $^\circ\text{C}$ , which is maintained for 3 h. The resulting product was obtained through centrifugation and was then subjected to multiple washes using water and ethanol.



## 2. RESULTS AND DISCUSSION

View Article Online  
DOI: 10.1039/D6YA00052E

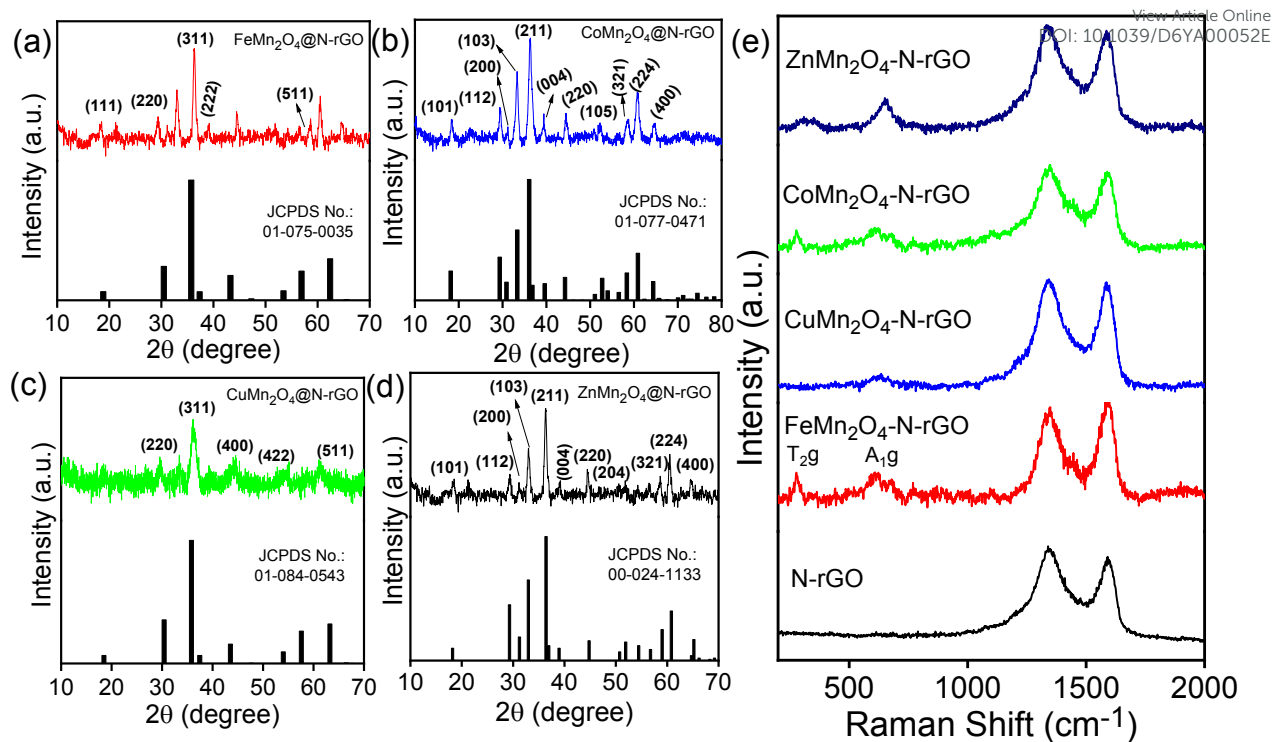
**Scheme 1.** Illustration for the synthesis of MMn<sub>2</sub>O<sub>4</sub> oxides (M= Fe, Co, Cu, and Zn) embedded over N-rGO.

As depicted in Scheme 1, a series of manganese-based spinel oxides was synthesized using GO, metal salts, PVP, aq. NH<sub>3</sub> via refluxing the mixtures under solvothermal reaction at 130°C for a duration of 3 h. (see Methods for details in ESI). Figure 1(a) shows the powder X-ray diffraction patterns (PXRD) for the bimetallic FeMn<sub>2</sub>O<sub>4</sub>, CoMn<sub>2</sub>O<sub>4</sub>, CuMn<sub>2</sub>O<sub>4</sub> and ZnMn<sub>2</sub>O<sub>4</sub> supported on N-rGO matched with JCPDS patterns of 01-075-0035, 01-077-0471, 01-004-0543 and 00-024-1133 respectively. For FeMn<sub>2</sub>O<sub>4</sub>, heterostructure exhibits characteristic peaks located at  $2\theta = 18.4, 30.1, 35.8, 38.2$  and  $56.8^\circ$  corresponding to the (111), (220), (311), (222) and (511) planes. For CoMn<sub>2</sub>O<sub>4</sub>, the peaks observed at  $2\theta = 18.2, 29.2, 30.8, 32.2, 36.09, 39.5, 44.4, 52.6, 58.3, 61.0$  and  $64.6^\circ$  corresponds to (101), (112), (200), (103), (211), (004), (220), (105), (321), (224), and (400) planes. For CuMn<sub>2</sub>O<sub>4</sub>, the peaks located



displays peaks at  $2\theta = 30.3, 35.6, 43.6, 54.4$  and  $63.3^\circ$  corresponds to (220), (311), (400), (422) and (511). Furthermore, the phase of  $\text{ZnMn}_2\text{O}_4$  was verified by peaks located at  $2\theta = 17.8, 29.3, 31.2, 33.0, 36.5, 39.1, 44.8, 59.0, 60.6$  and  $65.0^\circ$  corresponds to (101), (112), (200), (103), (211), (004), (204), (321), (224) and (400) planes respectively. These distinct diffraction patterns align with the crystallographic planes of spinel, confirming the successful synthesis and formation of the desired spinel structures. Notably, the peaks for  $\text{CuMn}_2\text{O}_4@\text{N-rGO}$  are noticeably less intense, attributed to several factors including lower crystallinity, smaller particle sizes, defects, or less ordered structures within the material. Figure S1 shows the PXRD pattern of the synthesized rGO. The depicted Raman spectra [Figure 1(b)] in the range from 200 to  $2000\text{ cm}^{-1}$  offer crucial insights into the vibrational and structural properties of the composites. Distinct peaks at  $277$  and  $618\text{ cm}^{-1}$  correspond to specific vibrational modes assigned to  $T_{2g}$  and  $A_{1g}$  arising from the symmetrical stretching of M–O bonds at tetrahedral positions within the spinel structure. Additionally, the Raman spectrum displays peaks at  $1347$  and  $1592\text{ cm}^{-1}$  known as the D and G bands of graphitic carbon. The D band typically signifies disorder within the graphene structure, while the G band indicates the presence of graphitic carbon. The intensity ratio of the D and G bands ( $I_D/I_G$ ) has been utilized to provide insights into the  $\text{sp}^2$  domain size and the partially ordered crystal structure of carbon. A lower  $I_D/I_G$  ratio generally indicates fewer defects and a higher degree of graphitization and structural integrity of the material. In this context, the reduced  $I_D/I_G$  ratio observed in  $\text{FeMn}_2\text{O}_4@\text{N-rGO}$  ( $\sim 0.87$ ) compared to  $\text{CuMn}_2\text{O}_4@\text{N-rGO}$  ( $\sim 1.05$ ),  $\text{CoMn}_2\text{O}_4@\text{N-rGO}$  ( $\sim 1.07$ ),  $\text{ZnMn}_2\text{O}_4@\text{N-rGO}$  ( $\sim 1.09$ ), and N-rGO ( $\sim 1.16$ ) suggests  $\text{FeMn}_2\text{O}_4@\text{N-rGO}$  has fewer defects (Table S1). Interestingly, the  $\text{FeMn}_2\text{O}_4@\text{N-rGO}$  heterostructure exhibited the lowest  $I_D/I_G$  ratio (0.87), suggesting that the Fe/Mn species, possibly promoting the degree of catalytic re-graphitization of the rGO carrier during the hydrothermal reaction, thereby enhancing the overall structural order and conductivity.

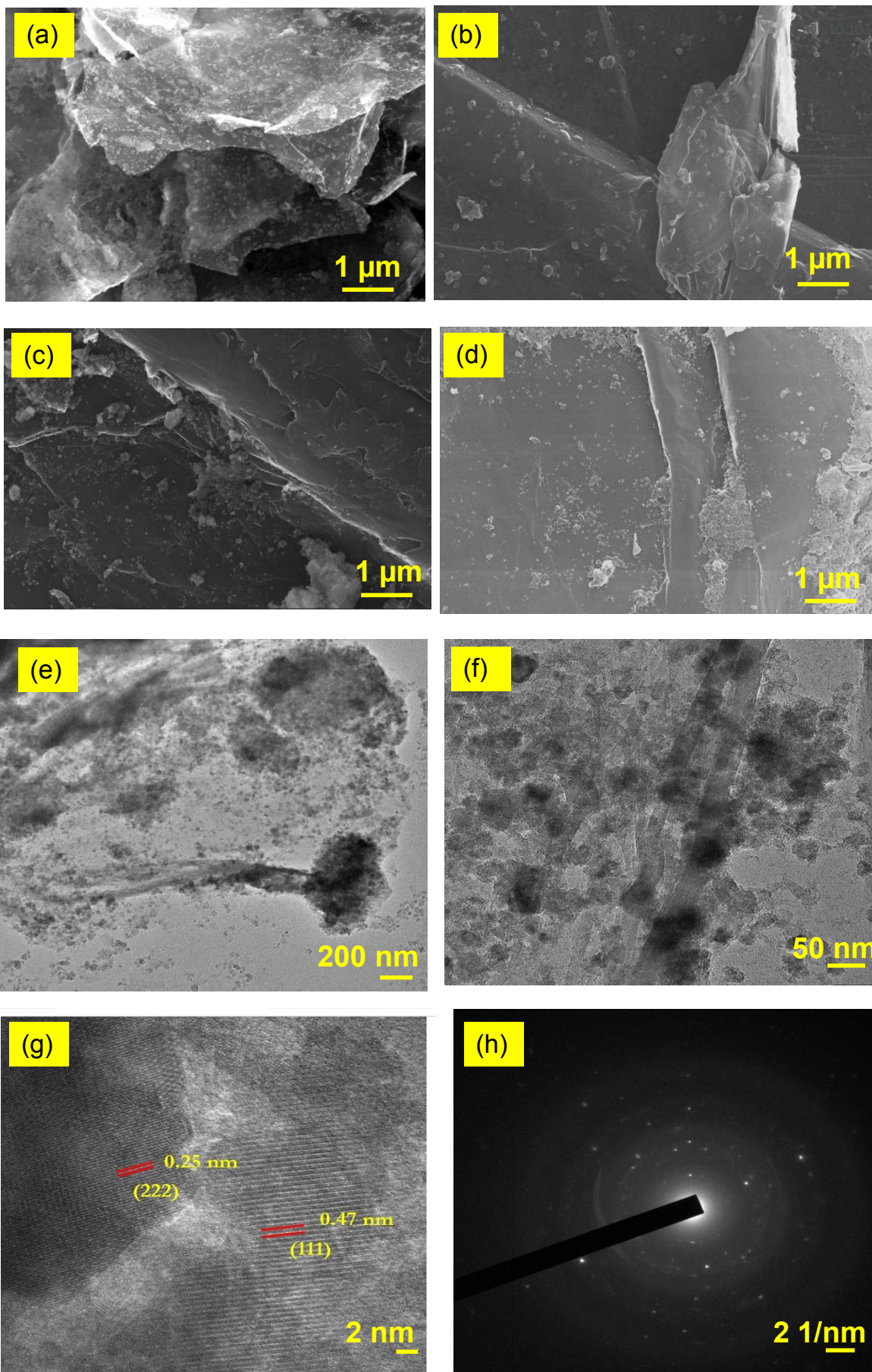
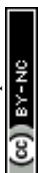




**Figure 1.** PXRD patterns (a) and Raman spectra (b) of  $MMn_2O_4$  oxides ( $M = Fe, Co, Cu,$  and  $Zn$ ) embedded over N-rGO.

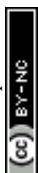
FT-IR spectra recorded for  $MMn_2O_4$  ( $M = Fe, Co, Cu,$  and  $Zn$ ) offer crucial insights into the molecular vibrations and functional groups present in Mn oxide spinel over N-rGO sheets (Figure S2). The C-O-C and -OH bending vibrations originating from carboxylic acid of rGO are represented by peaks at 1072 and 1412  $cm^{-1}$ . Additionally, the peak at 1275  $cm^{-1}$  corresponds to the C-N band and the peak at 1632  $cm^{-1}$  signifies C=O group. These specific functional groups act as binding sites for the stabilization of Mn oxide nanoparticles on the rGO support. Moreover, a prominent peak observed at 590  $cm^{-1}$ , is attributed to the metal-oxygen bonds in the  $MMn_2O_4$  structure.



New Article Online  
/D6YA00052E

**Figure 2.** SEM images of the  $\text{FeMn}_2\text{O}_4@\text{N-rGO}$  (a),  $\text{CoMn}_2\text{O}_4@\text{N-rGO}$  (b),  $\text{CuMn}_2\text{O}_4@\text{N-rGO}$  (c), and  $\text{ZnMn}_2\text{O}_4@\text{N-rGO}$  (d); TEM (e and h), HR-TEM (g), and SAED pattern (h) of the  $\text{FeMn}_2\text{O}_4@\text{N-rGO}$  heterostructures.

As shown in Figure 2 (a-d), the spherical particles are scattered across multi-layered rGO sheets, providing a rough texture. The SEM images exhibit a cluster of plate-like structures, indicating a layered configuration with jagged edges, and fewer cracks observed running through a rough and uneven surface, accompanied by assembly of particles in size ranging from 10 to 40 nm. For  $\text{FeMn}_2\text{O}_4@\text{N-rGO}$  (Figure 2a), homogeneous distribution of nanoparticles with minimal agglomeration over crumpled rGO sheets were observed. In  $\text{CoMn}_2\text{O}_4@\text{N-rGO}$  (Figure 2b), showed a compact rough surface morphology because of the particle-sheet interactions. The  $\text{CuMn}_2\text{O}_4@\text{N-rGO}$  heterostructures (Figure 2c) significant particle clustering along wrinkled rGO layers were observed which causing roughness. For  $\text{ZnMn}_2\text{O}_4@\text{N-rGO}$  (Figure 2d), the particles are less uniformly dispersed across rGO sheets, producing a planar texture with controlled particle growth over rGO layers. Furthermore, Figure 2e and 2f illustrate the transparent nature of stacked and corrugated rGO nanosheets, indicating structural flexibility. Furthermore, the surface and edges of the multi-layered rGO nanosheets are decorated with  $\text{FeMn}_2\text{O}_4$  nanoparticles with sizes ranging from 10-30 nm. Interestingly, these nanoparticles assemble at regular intervals on the rGO surface, without merging, showcasing the stabilizing nature of rGO. Additionally, the HRTEM image of the  $\text{FeMn}_2\text{O}_4$  nanoparticles unveils the lattice fringes spanning 0.25 and 0.45 nm, indicative of a spinel's (222) and (111) reflections (Figure 2g). The SAED pattern showed the poly-crystalline nature of  $\text{FeMn}_2\text{O}_4@\text{N-rGO}$  as shown in Figure 2h.



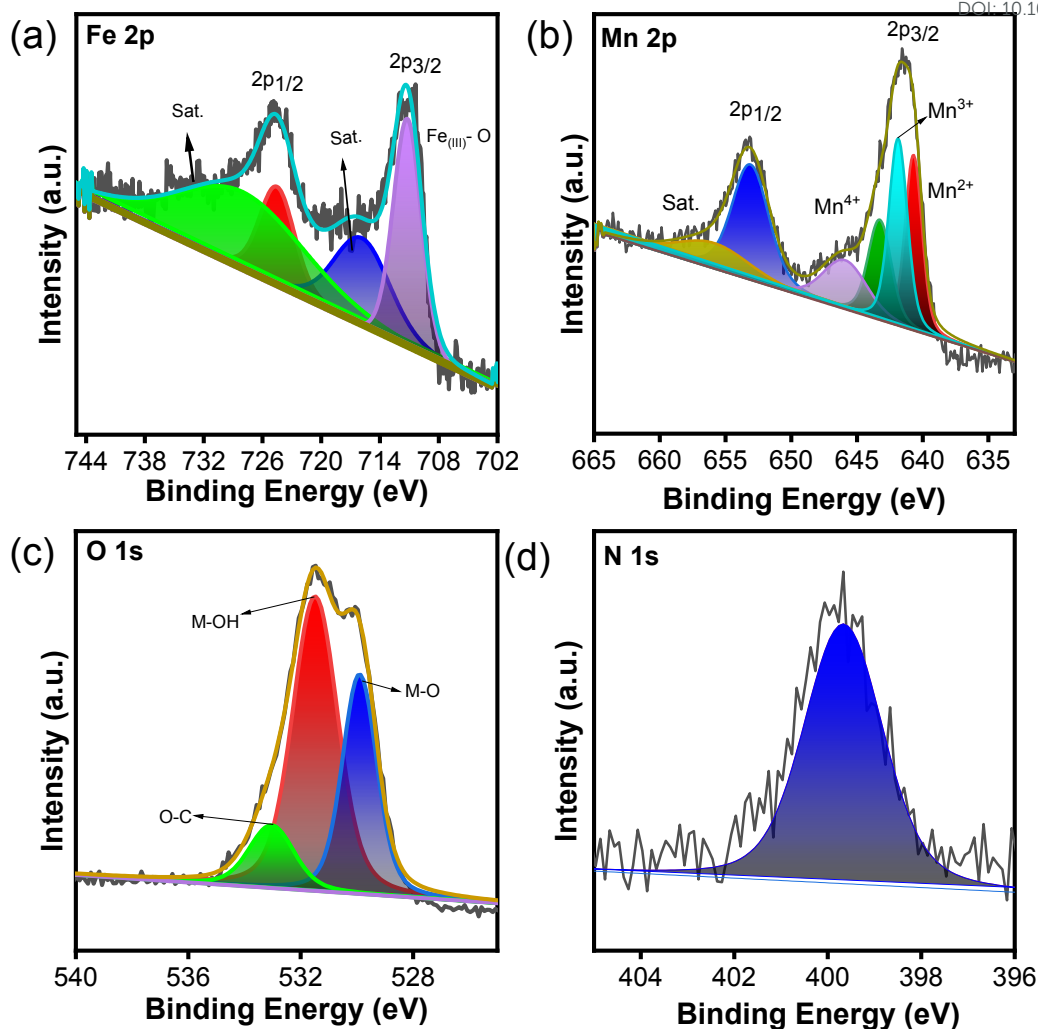


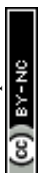
**Figure 3.** High-resolution XPS of Fe 2p (a), Mn 2p (b), O 1s (c), and N 1s (d) of FeMn<sub>2</sub>O<sub>4</sub>@N-rGO heterostructures.

The survey scan unveiled the presence of Fe, Mn, O, N and C elements with atomic percentages of 4.3, 8.0, 30.9, 1.2, and 55.6 respectively (Figure S3a). As shown in Figure 3a, the high-resolution Fe 2p scan, four peaks were observed. Iron is predominantly trivalent: the Fe 2p<sub>3/2</sub> main line at 711.2 eV and its spin-orbit partner at 724.9 eV together with pronounced shake-up satellites at 716.6 and 728.7 eV are diagnostic of Fe<sup>3+</sup> in oxide environment; no significant Fe<sup>2+</sup> 2p<sub>3/2</sub> peak is resolved, suggesting Fe is mainly Fe<sup>3+</sup> in the spinel lattice.<sup>[42, 43]</sup> As shown in Figure 3b, the XPS analysis of manganese exists in mixed oxidation states: the Mn 2p<sub>3/2</sub>



components at 640.7 and 641.8 eV are assigned to  $\text{Mn}^{2+}$  and  $\text{Mn}^{3+}$ , respectively, with a characteristic Mn  $2p_{3/2}$  shake-up near 646.0 eV and the  $2p_{1/2}$  partners observed at 653.2 (main) and 656.4 eV (satellite) respectively. An additional higher-binding feature at 643.2 eV is indicative of a minor  $\text{Mn}^{4+}$  contribution or a strongly oxidized surface species.<sup>[44-47]</sup> The spin-orbit splitting values were calculated to be 13.4 eV for Fe 2p and 11.5 eV for Mn 2p, which are consistent with reported literature, confirming the correct assignment of Fe and Mn oxidation states. Figure 3c displayed characteristic O 1s binding energies at 529.9, 531.4, and 532.9 eV attributed to metal oxide of Fe or Mn in the spinel network, lattice oxygen (metal-oxygen bond), and O–C bond originating from rGO support.<sup>[24, 48]</sup> Additionally, in Figure 3d, a binding energy of 399 eV corresponds to pyrrolic N, similar to that of nitrogen-doped rGO networks.<sup>[49, 50]</sup> The C 1s XP spectrum could be fitted into three Gaussian peaks at 284.7, 286, and 288.4 eV, corresponding to graphitic carbon (C–C), C–O, and C–N, respectively (Figure S3b). The detailed XPS analysis of  $\text{CuMn}_2\text{O}_4@\text{N-rGO}$ ,  $\text{CoMn}_2\text{O}_4@\text{N-rGO}$ , and  $\text{ZnMn}_2\text{O}_4@\text{N-rGO}$  are given in Supporting Information (Figure S4-S6). These XP spectra confirmed the elemental composition and oxidations states, binding energies of respective elements. This results further confirms integration of different metal oxides in N-doped rGO matrix.

Subsequently, CVs were conducted at a sweep rate of  $20 \text{ mV}\cdot\text{s}^{-1}$ , with the results depicted in Figure 4a. The CV curves of  $\text{FeMn}_2\text{O}_4@\text{N-rGO}$ ,  $\text{CoMn}_2\text{O}_4@\text{N-rGO}$ ,  $\text{CuMn}_2\text{O}_4@\text{N-rGO}$  and  $\text{ZnMn}_2\text{O}_4@\text{N-rGO}$  display distinct anodic and cathodic features within the potential window of 0.75–1.65 V vs RHE. All samples demonstrated a progressive rise in current density at higher potentials, indicating the onset of OER activity. Among the catalysts,  $\text{FeMn}_2\text{O}_4@\text{N-rGO}$  shows the highest anodic current density and earliest OER onset. As depicted in Figure 4b, the OER polarization curves for  $\text{MMn}_2\text{O}_4$  (M= Fe, Co, Cu, and Zn) bimetallic oxide NPs over N-rGO were studied, among which  $\text{FeMn}_2\text{O}_4\text{-N-rGO}$  demonstrated a significantly lower overpotential of 330 mV at a current density of  $10 \text{ mA}\cdot\text{cm}^{-2}$ . In contrast, the  $\text{CoMn}_2\text{O}_4@\text{N-rGO}$



rGO ( $\sim 390$  mV),  $\text{CuMn}_2\text{O}_4@N\text{-rGO}$  ( $\sim 440$  mV),  $\text{ZnMn}_2\text{O}_4@N\text{-rGO}$  ( $\sim 400$  mV) displayed higher overpotential ( $\eta_{\text{OER}}$ ) at  $\sim 10.0$   $\text{mA cm}^{-2}$ . Furthermore, the  $\text{FeMn}_2\text{O}_4$  and  $\text{FeMn}_2\text{O}_4@r\text{GO}$  electrodes exhibited the onset potentials of 1.64 and 1.62 V, respectively, with corresponding overpotentials of approximately 480 and 450 mV at  $10$   $\text{mA cm}^{-2}$ , as shown in Figure S7a. These findings underscore the critical role of rGO lattice with nitrogen doping, enhancing the catalytic activity as evidenced by the lower overpotentials and higher current densities.<sup>[37]</sup>

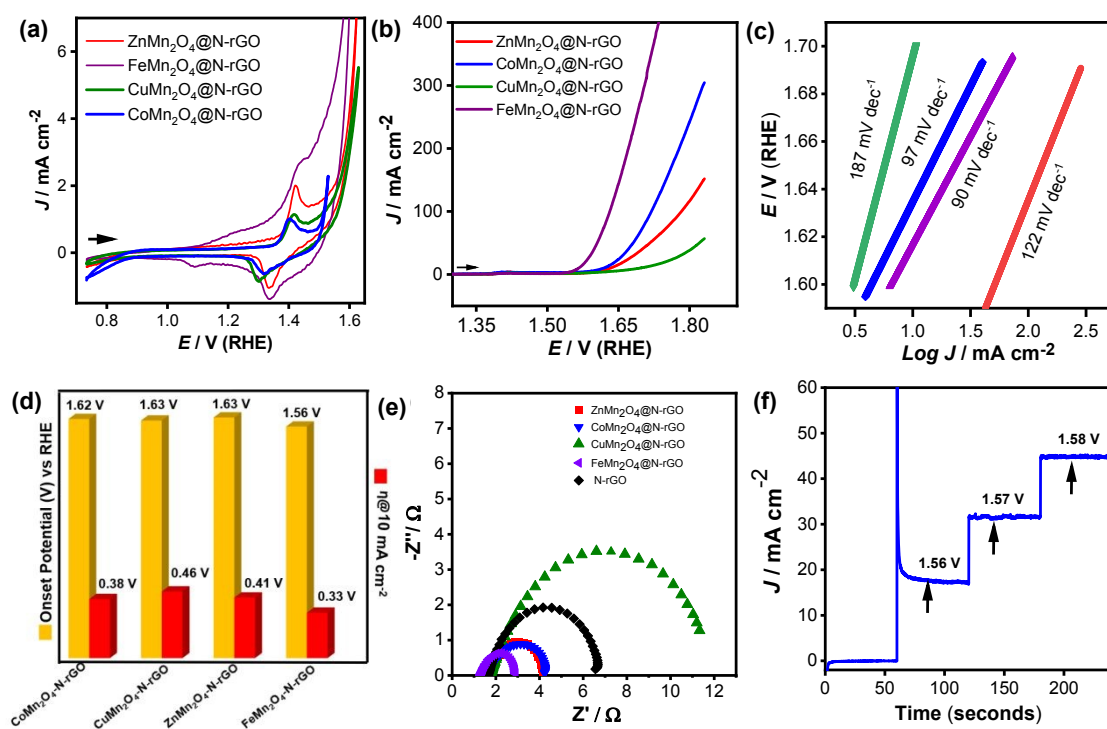


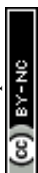
**Figure 4.** OER studies of the  $\text{MMn}_2\text{O}_4$  oxides ( $M = \text{Fe}, \text{Co}, \text{Cu}$  and  $\text{Zn}$ ) embedded over  $N\text{-rGO}$  in  $1.0$   $\text{M KOH}$ : CV (a), LSV (b), Tafel slope (c), plot of the onset and overpotential against the electrodes at  $10$   $\text{mA cm}^{-2}$  (d), EIS Nyquist plots recorded potentials corresponding to  $10$   $\text{mA cm}^{-2}$  for all the electrode materials (e) and stepwise chronoamperometry (f) of  $\text{FeMn}_2\text{O}_4\text{-N-rGO}$  heterostructures.

The kinetics of this reaction were further examined through corresponding Tafel plots [ $\eta$  versus  $\log(j)$ ], as illustrated in Figure 4c. Notably, the  $\text{FeMn}_2\text{O}_4@N\text{-rGO}$  catalyst exhibited a lower



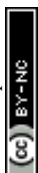
Tafel slope ( $90 \text{ mV}\cdot\text{dec}^{-1}$ ) compared to  $\text{CoMn}_2\text{O}_4@\text{N-rGO}$  ( $\sim 97 \text{ mV}\cdot\text{dec}^{-1}$ ),  $\text{CuMn}_2\text{O}_4@\text{N-rGO}$  ( $\sim 187 \text{ mV}\cdot\text{dec}^{-1}$ ), and  $\text{ZnMn}_2\text{O}_4@\text{N-rGO}$  ( $\sim 122 \text{ mV}\cdot\text{dec}^{-1}$ ), indicating superior electrokinetics compared to the rest of the electrocatalysts. Overall, the electrochemical assessment revealed that  $\text{FeMn}_2\text{O}_4@\text{N-rGO}$  exhibited superior electrocatalytic OER performance, displaying lower overpotential, higher current density, and improved electrokinetics compared to other compositions. Figure 4d presents a bar chart illustrating the onset potential and overpotential of the catalysts at a current density of  $10 \text{ mA cm}^{-2}$ . To further investigate the electrode kinetics and charge transfer capabilities, Electrochemical Impedance Spectroscopy (EIS) was performed. As shown in Figure 4e, the Nyquist plots were recorded at the specific potentials corresponding to a current density of  $10 \text{ mA cm}^{-2}$  for each catalyst. Specifically, the applied potentials were  $0.55 \text{ V}$  for  $\text{FeMn}_2\text{O}_4@\text{N-rGO}$ ,  $0.60 \text{ V}$  for  $\text{CoMn}_2\text{O}_4@\text{N-rGO}$ ,  $0.61 \text{ V}$  for  $\text{ZnMn}_2\text{O}_4@\text{N-rGO}$ ,  $0.64 \text{ V}$  for N-rGO, and  $0.68 \text{ V}$  for  $\text{CoMn}_2\text{O}_4@\text{N-rGO}$  (vs. Ref Electrode – Ag/AgCl). Among the studied materials, the  $\text{FeMn}_2\text{O}_4@\text{N-rGO}$  electrode exhibited the smallest semicircle diameter, indicating the lowest charge transfer resistance  $R_{ct}$ . This superior electronic conductivity is attributed to the synergistic effect between the  $\text{FeMn}_2\text{O}_4$  nanoparticles and the highly conductive N-rGO framework. As shown in Figure 4f, the multi-step chronopotentiometric curve of the  $\text{FeMn}_2\text{O}_4@\text{N-rGO}$  electrode indicates excellent mass transport properties, considerable electrical conductivity, and remarkable structural stability. As displayed in Figure S7b and 7c, the plot of anodic and cathodic peak current densities ( $j$ ) against the square root of scan rates showed a linear relationship, indicating that the electrode processes are diffusion controlled.

Figure S8a shows the HER polarization curves for  $\text{MMn}_2\text{O}_4$  (where  $M = \text{Fe, Co, Cu, and Zn}$ ) nanoparticles embedded over N-rGO. Among the catalysts tested,  $\text{FeMn}_2\text{O}_4@\text{N-rGO}$  exhibited the lowest overpotential at approximately  $153 \text{ mV}$  at  $-10 \text{ mAcm}^{-2}$ , indicating its superior HER activity in compare to other electrodes developed in this study. The  $\text{CoMn}_2\text{O}_4@\text{N-rGO}$



exhibited closely with an overpotential of about 164 mV at  $-10 \text{ mAcm}^{-2}$ ,  $\text{CuMn}_2\text{O}_4@\text{N-rGO}$  required a slightly higher overpotential of around 170 mV at  $-10 \text{ mAcm}^{-2}$ , while  $\text{ZnMn}_2\text{O}_4@\text{N-rGO}$  displayed the highest overpotential among the tested materials, with 179 mV at  $-10 \text{ mAcm}^{-2}$ . The kinetics of this reaction were further examined through corresponding Tafel plots ( $\eta$  versus  $\log(j)$ ), as illustrated in Figure S8b. Notably, the  $\text{FeMn}_2\text{O}_4@\text{N-rGO}$  catalyst exhibited a lower Tafel slope ( $\sim 90 \text{ mV.dec}^{-1}$ ) compared to other  $\text{CoMn}_2\text{O}_4@\text{N-rGO}$  ( $\sim 91 \text{ mV.dec}^{-1}$ ),  $\text{CuMn}_2\text{O}_4@\text{N-rGO}$  ( $\sim 151 \text{ mV.dec}^{-1}$ ), and  $\text{ZnMn}_2\text{O}_4@\text{N-rGO}$  ( $\sim 93 \text{ mV.dec}^{-1}$ ), indicating superior electrode kinetics compared to other electrocatalysts. The enhanced HER performance of these catalysts can be attributed to the synergistic effects of the bimetallic oxide composition and the nitrogen-doped reduced graphene oxide support. [51, 52] The nitrogen doping enhances the electronic conductivity, providing additional active sites for the HER, while reduced graphene oxide lattice offers conductivity thus facilitating efficient charge transfer.

High-resolution Mn 2p XP spectra and proposed mechanism (Figure S9) confirm the coexistence of  $\text{Mn}^{2+}/\text{Mn}^{3+}/\text{Mn}^{4+}$  species, with  $\text{Mn}^{3+}$  dominant in all heterostructures which helps during OER. In addition to factors such as catalyst size, morphology, conductivity, and the exposure of active sites, the surface wettability of the electrocatalyst significantly influences the interaction between the electrolyte and the electrode surface. We assessed the water-wetting ability of both the supported  $\text{FeMn}_2\text{O}_4@\text{N-rGO}/\text{NF}$  electrode and the bare NF electrode by measuring their water contact angles (Figure S10a and 10b). The rGO-supported  $\text{FeMn}_2\text{O}_4@\text{N-rGO}/\text{NF}$  material demonstrated a higher water wettability with a contact angle of  $0.6^\circ$ , compared to the supportless bare NF, which had a contact angle of  $130^\circ$ . This improved hydrophilicity enhances the charge transfer rate between the electrolyte and the electrode facilitating effective conduction, thereby reducing ohmic losses and boosting the OER activity of  $\text{FeMn}_2\text{O}_4-\text{N-rGO}$ . The double-layer capacitance ( $C_{dl}$ ), which is directly related to the electrochemically active surface area (Figure S10c and 10d) was investigated. A higher  $C_{dl}$



indicates a larger ECSA, which in turn suggests more accessible active sites for catalytic reactions. The  $C_{dl}$  of the  $\text{FeMn}_2\text{O}_4@\text{N-rGO}$  electrode was calculated to be  $80 \text{ mF cm}^{-2}$ , revealing that the  $\text{FeMn}_2\text{O}_4@\text{N-rGO}$  electrode possesses a substantial ECSA, providing a large number of accessible active sites. In this study, the  $\text{FeMn}_2\text{O}_4\text{-N-rGO}$  electrode demonstrated the highest TOF value of approximately  $3.0 \text{ s}^{-1}$ , indicating superior catalytic activity compared to other tested electrodes (Figure S11). For comparison, the TOF values for  $\text{ZnMn}_2\text{O}_4@\text{N-rGO}$ ,  $\text{CoMn}_2\text{O}_4@\text{N-rGO}$ , and  $\text{CuMn}_2\text{O}_4@\text{N-rGO}$  were significantly lower,  $\sim 0.6$ ,  $\sim 1.1$ , and  $\sim 1.0 \text{ s}^{-1}$ , respectively. The high TOF value of the  $\text{FeMn}_2\text{O}_4@\text{N-rGO}$  electrode suggests a greater number of catalytic reactions attributed to its enhanced electrochemical properties. In terms of moles of active sites, the  $\text{FeMn}_2\text{O}_4@\text{N-rGO}$  electrode has approximately 0.14 moles of active sites, whereas the  $\text{ZnMn}_2\text{O}_4@\text{N-rGO}$ ,  $\text{CoMn}_2\text{O}_4@\text{N-rGO}$ , and  $\text{CuMn}_2\text{O}_4@\text{N-rGO}$  electrodes possessed around 0.04, 0.05, and 0.06 moles, respectively. The interconnected flow of high TOF values and large  $C_{dl}$  reveals the superior performance of the  $\text{FeMn}_2\text{O}_4\text{-N-rGO}$  electrode. The greater number of accessible active sites facilitated by a high ECSA, enabling more efficient catalytic reactions, as reflected in its higher TOF. This synergy between TOF and ECSA highlights the importance of optimizing both intrinsic catalytic activity and the physical properties of the electrode material enhancing overall electrocatalytic performance. A comparative summary of onset potentials, overpotentials, and active site densities is listed in Table S1 (Refer SI).

New Article Online  
DOI: 10.1039/D6TA00052E



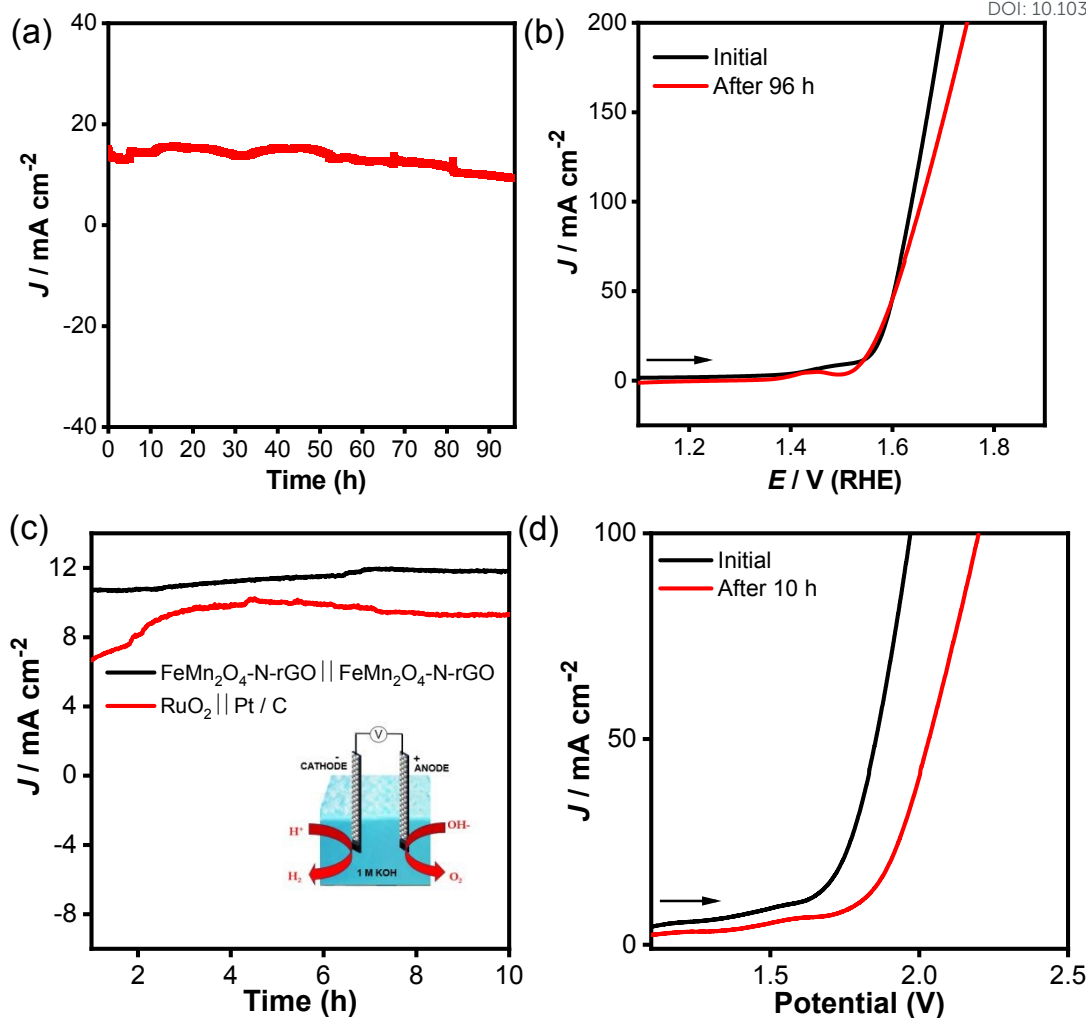


**Figure 5.** Amperometric curves of the FeMn<sub>2</sub>O<sub>4</sub>@N-rGO recorded at the constant applied potential of 1.56 V vs RHE (a); OER polarization curves of the FeMn<sub>2</sub>O<sub>4</sub>@N-rGO electrode recorded in 1.0 M KOH before (black curve) and after a stability test (red curve) (b); Chronoamperometric (c) and LSV (d) curves of the FeMn<sub>2</sub>O<sub>4</sub>@N-rGO || FeMn<sub>2</sub>O<sub>4</sub>@N-rGO (black curve), and RuO<sub>2</sub>||Pt/C (red) couple for overall water splitting.

These tests were carried out in 1 M KOH to assess the durability of the sample under alkaline conditions. Following the stability tests, we assembled and tested the overall water electrolyser to evaluate its performance. The stability of the FeMn<sub>2</sub>O<sub>4</sub>@N-rGO catalyst was tested by evaluating its performance in the alkaline water electrolysis of water over a 96 h. The



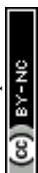
chronoamperometry (I vs t) test for the FeMn<sub>2</sub>O<sub>4</sub>@N-rGO catalyst was carried out, and the obtained response is displayed in Figure 5a. During the durability test, the overpotential of the FeMn<sub>2</sub>O<sub>4</sub>@N-rGO electrode didn't considerably increase, inferring good electrochemical stability in Figure 5b. The bi-functional FeMn<sub>2</sub>O<sub>4</sub>@N-rGO || FeMn<sub>2</sub>O<sub>4</sub>@N-rGO pair achieved a higher steady-state current density of approximately 7.9 mA cm<sup>-2</sup>. Additionally, a lower cell voltage of ~ 1.57 V to reach the current density of 10 mA cm<sup>-2</sup> was observed. In comparison, the conventional Pt/C || RuO<sub>2</sub> couple exhibited performance under similar conditions, as shown in Figures 5(c) and 5(d). This indicates that the FeMn<sub>2</sub>O<sub>4</sub>@N-rGO electrodes not only enhance the electrochemical reaction kinetics but also provide superior efficiency in electrochemical water splitting, highlighting their potential as effective and durable alternatives to traditional noble metal-based catalysts.<sup>[53]</sup>

According to the method reported in the literature<sup>[54]</sup>, The energy efficiency  $\eta$  of the FeMn<sub>2</sub>O<sub>4</sub>@N-rGO was determined at a current density of 10 mA cm<sup>2</sup> with the help of thermodynamic water-splitting potential of 1.23 V as the reference and applied below equation (1)

$$\eta = \frac{E_{f,o}}{V_{e,i}} \quad 1$$

Where, theoretical water-splitting potential  $E_{f,o} = 1.23$  V;  $V_{e,i}$  is the input voltage required to drive the electrolysis at  $j = 10$  mA cm<sup>-2</sup>. For the electrode with a mass loading of 3 mg cm<sup>-2</sup>, an input voltage of 1.57 V was required, resulting in a calculated energy efficiency of 78.3% without iR correction.

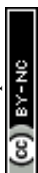
In order to test the changes/retention, the post-catalytic nanoparticle characterization to examine these changes were performed by using XPS and FE-SEM analyses. XPS analysis of FeMn<sub>2</sub>O<sub>4</sub>@N-rGO before and after, alkaline OER occurring through iron and manganese redox reactions which leads to restructuring of the surface (Figure S12). At the beginning, the



spinel structure has mixed-valent  $\text{Mn}^{2+}/\text{Mn}^{3+}$  and  $\text{Fe}^{2+}/\text{Fe}^{3+}$  states, which are essential for redox and electron conductivity. Once the OER process is initiated, the Fe 2p spectra (Figure S12a) reveal a significant rise in  $\text{Fe}^{3+}$  character, indicating oxidation of  $\text{Fe}^{2+}$  to  $\text{Fe}^{3+}$  and the formation of Fe-OOH-like surface layers. At the same time, there is an increase in  $\text{Mn}^{3+}$  observed from Mn 2p spectra, revealing the appearance of Mn-OOH (Figure S12b). The O 1s spectra displayed enhanced signals corresponding to hydroxides and oxyhydroxide species after OER, consistent with the formation of Fe-OH and Mn-OH surface groups. (Figure S12c). These changes reflect a synergistic redox evolution where both Fe and Mn participate in charge transfer and oxygen binding, crucial for catalytic activity. The enrichment of  $\text{Fe}^{3+}$  and  $\text{Mn}^{3+}$  species increases the density of active sites and facilitates lattice oxygen involvement, thereby accelerating the OER kinetics.<sup>[55-57]</sup> Furthermore, to assess the structural robustness, FE-SEM images were taken after 50 h durability. FE-SEM (Figure S13) confirmed that the  $\text{FeMn}_2\text{O}_4@\text{N-rGO}$  intimate contact with support were preserved without noticeable detachment. We benchmarked our catalyst against state-of-the-art OER catalysts, emphasizing their respective synthetic conditions. As summarized in Table S2, our material  $\text{FeMn}_2\text{O}_4\text{-N-rGO}$  heterostructure electrodes was prepared within remarkably short time scales and at low temperatures, yet it delivers strong OER activity in alkaline media, outperforming several existing reports.

## Conclusion

In summary, a series of transition metal cation-substituted manganese oxides ( $\text{MMn}_2\text{O}_4$ , where M = Co, Cu, Fe, and Zn) supported on nitrogen-doped reduced graphene oxide (N-rGO) nanosheets ( $\text{M-Mn}_2\text{O}_4@\text{N-rGO}$ ) heterostructures are developed using a facile solvothermal synthetic strategy. The variation in metal cations within the  $\text{M-Mn}_2\text{O}_4@\text{N-rGO}$  structure has been shown to significantly influence the OER activity in alkaline conditions. Among the tested materials, the  $\text{FeMn}_2\text{O}_4@\text{N-rGO}$  heterostructures exhibited the most



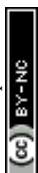
promising OER performance, with a low overpotential of 330 mV at a current density of 10 mA cm<sup>-2</sup>, highlighting their potential as a highly efficient electrocatalyst. Furthermore, the FeMn<sub>2</sub>O<sub>4</sub>@N-rGO catalyst demonstrated remarkable electrochemical stability, maintaining its performance over 96 h in 1 M KOH solution. Beyond OER, FeMn<sub>2</sub>O<sub>4</sub>@N-rGO also demonstrated excellent HER activity, delivering a low overpotential of ~153 mV at -10 mA cm<sup>-2</sup>, attributed to the coexistence of Fe<sup>3+</sup>/Fe<sup>2+</sup> and Mn<sup>3+</sup>/Mn<sup>4+</sup> redox couples that provide multiple electron transfer pathways. Importantly, the Mn<sup>3+</sup> ion contributes to a more balanced Mn-O octahedral geometry, enhancing electron overlap and facilitating intermediate adsorption. When assembled as a bifunctional electrode for overall water splitting (FeMn<sub>2</sub>O<sub>4</sub>@N-rGO serving as both anode and cathode), the system achieved a cell voltage of 1.57 V at 10 mA cm<sup>-2</sup> with operational stability over 10 h. These findings underscore the importance of cationic fine-tuning in manganese spinel oxides to enhance both OER and HER activities, paving the way for advanced bifunctional catalysts in energy conversion applications.

### Acknowledgements:

Authors acknowledge DST-SERB (CRG/2022/002686) for the financial assistance to this project and thank DST-FIST, Department of Chemistry, SRMIST. The central facilities at SRMIST and the Nanotechnology Research Centre (NRC), SRMIST, are gratefully acknowledged for providing the characterization facilities.

### Supporting Information:

Supporting information contains detailed materials and methods, physical and electrochemical characterization details, calculation methods, XRD of synthesised GO, FT-IR and spectra of MMn<sub>2</sub>O<sub>4</sub> oxides (M= Fe, Co, Cu and Zn) embedded over N-rGO,



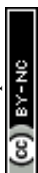
Survey scan and HR- XP spectra of C 1s of FeMn<sub>2</sub>O<sub>4</sub>@N-rGO heterostructures, HR-XP spectra of CuMn<sub>2</sub>O<sub>4</sub>@N-rGO, CoMn<sub>2</sub>O<sub>4</sub>@N-rGO and ZnMn<sub>2</sub>O<sub>4</sub>@N-rGO heterostructures, LSV curves of N-rGO, FeMn<sub>2</sub>O<sub>4</sub>, FeMn<sub>2</sub>O<sub>4</sub>@rGO and FeMn<sub>2</sub>O<sub>4</sub>@N-rGO. HER polarization curves and Tafel analysis of MMn<sub>2</sub>O<sub>4</sub> (M = Fe, Co, Cu, and Zn) oxides embedded on N-rGO, HR- XP spectra overlap of MMn<sub>2</sub>O<sub>4</sub> oxides (M= Fe, Co, Cu and Zn) embedded over N-rGO, Proposed OER mechanism, Water contact angle measurement, ECSA of FeMn<sub>2</sub>O<sub>4</sub>@N-rGO heterostructures, Isolated cathodic (reduction) peaks extracted from the CV curves of MMn<sub>2</sub>O<sub>4</sub> oxides (M= Fe, Co, Cu and Zn) embedded over N-rGO, HR-XPS after and before OER of the FeMn<sub>2</sub>O<sub>4</sub>@N-rGO heterostructures, Summary of OER activity metrics of prepared electrocatalyst, Comparative OER performance of FeMn<sub>2</sub>O<sub>4</sub>-N-rGO heterostructures with recently reported electrocatalysts.

### Author Contribution

**M. I and A. S:** Catalyst Synthesis, Physical and Electrochemical characterization, Stability testing, Data curation, First draft, **G.M and K. K. R. D:** Supervision, Project administration, Funding acquisition, Writing – review & editing.

### Conflict of Interest:

There is no conflict of interest to declare



## References

- [1] B. Zhu, C. Wei, A Green Hydrogen Era: Hope or Hype?, *Environmental Science & Technology* **2022**, *56*, 11107-11110
- [2] X. Li, L. Zhao, J. Yu, X. Liu, X. Zhang, H. Liu, W. Zhou, Water Splitting: From Electrode to Green Energy System, *Nano-Micro Letters* **2020**, *12*, 131
- [3] I. Vincent, D. Bessarabov, Low cost hydrogen production by anion exchange membrane electrolysis: A review, *Renewable and Sustainable Energy Reviews* **2018**, *81*, 1690-1704
- [4] J. C. Ehlers, A. A. Feidenhans'l, K. T. Therkildsen, G. O. Larrazábal, Affordable Green Hydrogen from Alkaline Water Electrolysis: Key Research Needs from an Industrial Perspective, *ACS Energy Letters* **2023**, *8*, 1502-1509
- [5] A. A. Feidenhans'l, Y. N. Regmi, C. Wei, D. Xia, J. Kibsgaard, L. A. King, Precious Metal Free Hydrogen Evolution Catalyst Design and Application, *Chemical Reviews* **2024**, *124*, 5617-5667
- [6] S. Li, S. Zhao, F. Hu, L. Li, J. Ren, L. Jiao, S. Ramakrishna, S. Peng, Exploring the potential Ru-based catalysts for commercial-scale polymer electrolyte membrane water electrolysis: A systematic review, *Progress in Materials Science* **2024**, *145*, 101294
- [7] S. Anantharaj, S. R. Ede, K. Sakthikumar, K. Karthick, S. Mishra, S. Kundu, Recent Trends and Perspectives in Electrochemical Water Splitting with an Emphasis on Sulfide, Selenide, and Phosphide Catalysts of Fe, Co, and Ni: A Review, *ACS Catalysis* **2016**, *6*, 8069-8097
- [8] X. Zhang, Z. Zuo, C. Liao, F. Jia, C. Cheng, Z. Guo, Strategies for Designing Advanced Transition Metal-Based Electrocatalysts for Alkaline Water/Seawater Splitting at Ampere-Level Current Densities, *ACS Catalysis* **2024**, *14*, 18055-18071
- [9] Giddaerappa, K. Naseem, K. Sharath, M. Hojamberdiev, L. K. Sannegowda, Substrate-Driven Electrocatalysis of Natural and Earth-Abundant Pyrite Towards Oxygen Evolution Reaction, *Electrochimica Acta* **2024**, *475*, 143575
- [10] N. Kousar, G. Patil, A. C. Kumbara, B. Nisty, R. G. H, L. K. Sannegowda, Engineering of abundant metal complexes for electrochemical water splitting, *Dalton Transactions* **2025**, *54*, 12714-12736
- [11] V. K, K. G. K, S. R. Ananda, L. K. Sannegowda, S. Aralekallu, A ligand-specific bimetallic electrocatalyst for efficient oxygen evolution reaction at higher current density, *Sustainable Energy & Fuels* **2025**, *9*, 2287-2293
- [12] G. Maduraiveeran, P. Kannan, A. S. Alnaser, Earth-abundant nanomaterials for electrolytic hydrogen production: Advances, mechanistic insights, and industrial prospects, *Renewable and Sustainable Energy Reviews* **2026**, *231*, 116750
- [13] S. Karuppuchamy, T. A. Kumaravelu, T. T. Thuy Nga, C.-L. Chen, T.-S. Chan, C.-L. Dong, D. Arumugam, S. Ramasamy, M. Govindasamy, C.-Y. Kuo, S. Thangavelu, Tailored Cobalt Single Atoms on Strong Metal-Support Interactions Drive the Tandem Bifunctional Electrocatalytic Overall Water Splitting, *ACS Applied Energy Materials* **2025**, *8*, 11099-11114
- [14] K. M. Nair, S. Thangavelu, MOF-Derived ZrS<sub>2</sub>/ZrO<sub>2</sub> Nanosheet Arrays Enable Cationic Modulation for Low-Overpotential Electrocatalytic Overall Water Splitting, *Energy & Fuels* **2025**, *39*, 13658-13673
- [15] X.-M. Liu, X. Cui, K. Dastafkan, H.-F. Wang, C. Tang, C. Zhao, A. Chen, C. He, M. Han, Q. Zhang, Recent advances in spinel-type electrocatalysts for bifunctional oxygen reduction and oxygen evolution reactions, *Journal of Energy Chemistry* **2021**, *53*, 290-302
- [16] C. Rong, X. Huang, H. Arandiyani, Z. Shao, Y. Wang, Y. Chen, Advances in Oxygen Evolution Reaction Electrocatalysts via Direct Oxygen-Oxygen Radical Coupling Pathway, *Advanced Materials* *n/a*, 2416362



- [17] Q. Zhao, Z. Yan, C. Chen, J. Chen, Spinel: Controlled Preparation, Oxygen Reduction/Evolution Reaction Application, and Beyond, *Chemical Reviews* **2017**, *117*, 10121-10211
- [18] J. O. Olowoyo, R. J. Kriek, Recent Progress on Bimetallic-Based Spinel as Electrocatalysts for the Oxygen Evolution Reaction, *Small* **2022**, *18*, 2203125
- [19] Ö. N. Avci, L. Sementa, A. Fortunelli, Mechanisms of the Oxygen Evolution Reaction on NiFe<sub>2</sub>O<sub>4</sub> and CoFe<sub>2</sub>O<sub>4</sub> Inverse-Spinel Oxides, *ACS Catalysis* **2022**, *12*, 9058-9073
- [20] X. Gao, H. Zhang, Q. Li, X. Yu, Z. Hong, X. Zhang, C. Liang, Z. Lin, Hierarchical NiCo<sub>2</sub>O<sub>4</sub> Hollow Microcuboids as Bifunctional Electrocatalysts for Overall Water-Splitting, *Angewandte Chemie International Edition* **2016**, *55*, 6290-6294
- [21] Y. Wang, L. Chen, H. Zhang, M. Humayun, J. Duan, X. Xu, Y. Fu, M. Bououdina, C. Wang, Elaborately tailored NiCo<sub>2</sub>O<sub>4</sub> for highly efficient overall water splitting and urea electrolysis, *Green Chemistry* **2023**, *25*, 8181-8195
- [22] X. Zhu, Z. Ji, W. Wan, Y. Zhu, X. Lang, Q. Jiang, Vacancy-rich heterogeneous MnCo<sub>2</sub>O<sub>4.5</sub>@NiS electrocatalyst for highly efficient overall water splitting, *Journal of Colloid and Interface Science* **2025**, *678*, 878-884
- [23] P. C. Nagajyothi, K. Pavani, R. Ramaraghavulu, J. Shim, Microwave synthesis of NiMn<sub>2</sub>O<sub>4</sub>/Ni-foam: Efficient bifunctional electrocatalysts for overall water splitting, *International Journal of Hydrogen Energy* **2024**, *54*, 691-699
- [24] I. Madakannu, I. Patil, B. A. Kakade, K. R. D. Kasibhatta, Boosting oxygen evolution reaction performance by nickel substituted cobalt-iron oxide nanoparticles embedded over reduced graphene oxide, *Materials Chemistry and Physics* **2020**, *252*, 123238
- [25] I. Karakaya Durukan, Ö. Dag, Electronic Synergistic Effects on the Stability and Oxygen Evolution Reaction Efficiency of the Mesoporous LiMn<sub>2-x</sub>MxO<sub>4</sub> (M = Mn, Fe, Co, Ni, and Cu) Electrodes, *Inorganic Chemistry* **2024**, *63*, 22239-22257
- [26] Y. Zhou, Z. Zhou, L. Hu, R. Tian, Y. Wang, H. Arandiyani, F. Chen, M. Li, T. Wan, Z. Han, Z. Ma, X. Lu, C. Cazorla, T. Wu, D. Chu, A facile approach to tailor electrocatalytic properties of MnO<sub>2</sub> through tuning phase transition, surface morphology and band structure, *Chemical Engineering Journal* **2022**, *438*, 135561
- [27] S. Kong, A. Li, J. Long, K. Adachi, D. Hashizume, Q. Jiang, K. Fushimi, H. Ooka, J. Xiao, R. Nakamura, Acid-stable manganese oxides for proton exchange membrane water electrolysis, *Nature Catalysis* **2024**, *7*, 252-261
- [28] P. Wang, S. Zhang, Z. Wang, Y. Mo, X. Luo, F. Yang, M. Lv, Z. Li, X. Liu, Manganese-based oxide electrocatalysts for the oxygen evolution reaction: a review, *Journal of Materials Chemistry A* **2023**, *11*, 5476-5494
- [29] M. Guo, R. Deng, C. Wang, Q. Zhang, Recent progress of advanced manganese oxide-based materials for acidic oxygen evolution reaction: Fundamentals, performance optimization, and prospects, *Journal of Energy Chemistry* **2023**, *78*, 537-553
- [30] A. Goswami, D. Ghosh, D. Pradhan, K. Biradha, In Situ Grown Mn(II) MOF upon Nickel Foam Acts as a Robust Self-Supporting Bifunctional Electrode for Overall Water Splitting: A Bimetallic Synergistic Collaboration Strategy, *ACS Applied Materials & Interfaces* **2022**, *14*, 29722-29734
- [31] Y. S. S. Sarma, A. Ghosh, M. Jaiswal, S. S. Bhattacharya, S. Ramaprabhu, A spinel based high entropy oxide (Co, Fe, Mn, Ni, Li)<sub>3</sub>O<sub>4</sub> and reduced graphene oxide composite anode for seawater electrolysis, *International Journal of Hydrogen Energy* **2025**, *130*, 54-63
- [32] L. Liu, H. Huang, J. Tai, X. Wu, Z. Guo, X. Shen, S. Cui, X. Chen, The catalytic activity of reduced graphene aerogel anchored with CoFe<sub>2</sub>O<sub>4</sub> spinel via self-assembly technique for enhanced oxygen evolution reaction, *Carbon* **2024**, *219*, 118847
- [33] R. Miao, J. He, S. Sahoo, Z. Luo, W. Zhong, S.-Y. Chen, C. Guild, T. Jafari, B. Dutta, S. A. Cetegen, M. Wang, S. P. Alpay, S. L. Suib, Reduced Graphene Oxide Supported Nickel-Manganese-Cobalt Spinel Ternary Oxide Nanocomposites and Their Chemically Converted

View Article Online  
DOI: 10.1039/D6YA00052E



Sulfide Nanocomposites as Efficient Electrocatalysts for Alkaline Water Splitting, *ACS Catalysis* **2017**, *7*, 819-832 View Article Online  
DOI: 10.1039/D6YA00052E

- [34] Y. Yim, C. J. Park, Y. Lee, M. H. Kim, High-entropy spinel oxide (Mn<sub>0.5</sub>Co<sub>0.9</sub>Cr<sub>0.9</sub>Rh<sub>0.5</sub>Fe<sub>0.2</sub>)O<sub>4</sub> nanotubes: Cr-driven disorder engineering for enhanced oxygen evolution reaction, *Journal of Alloys and Compounds* **2025**, *1043*, 184248
- [35] B. Du, J. Zeng, R. Tang, Y. Li, Q. Hao, F. Wang, L. Liang, H. Liu, High-entropy spinel (FeCoNiMnCr)<sub>3</sub>O<sub>4</sub> nanoparticles supported on carbon nanotubes for enhanced electrochemical seawater oxidation, *Chemical Communications* **2025**, *61*, 15614-15617
- [36] M. D. Albaqami, M. U. Nisa, S. Mohammad, J. Hussain Shah, A. U. Rehman Baloch, A. G. Abid, S. Saleem, Phosphorus-Doped CuMn<sub>2</sub>O<sub>4</sub> Nanoflakes: A Highly Performed Electrocatalyst for Oxygen Evolution Reaction and Hydrogen Evolution Reaction in an Alkaline Environment, *Energy & Fuels* **2024**, *38*, 15533-15542
- [37] Y. Hu, X. Zhao, F. Li, Q. Dong, B. Wen, D. Sun, W. Liang, X. Lyu, Spherical ZnFe<sub>2</sub>O<sub>4</sub> Nanoparticles on Nitrogen-Doped Graphene: A Synergistic Effect on Efficient Electrocatalytic Oxygen Evolution Reaction, *ACS Applied Energy Materials* **2023**, *6*, 9985-9993
- [38] W. Zheng, M. Liu, L. Y. S. Lee, Best Practices in Using Foam-Type Electrodes for Electrocatalytic Performance Benchmark, *ACS Energy Letters* **2020**, *5*, 3260-3264
- [39] C. Qi, Q. Liu, Y. Dong, G. Zhang, X. Jiang, D. Gao, Quenching-induced surface reconstruction of FeMn<sub>2</sub>O<sub>4</sub> for promoted oxygen evolution reaction, *Journal of Alloys and Compounds* **2023**, *967*, 171754
- [40] R. Nandan, G. Raj, K. K. Nanda, FeCoNiMnCr High-Entropy Alloy Nanoparticle-Grafted NCNTs with Promising Performance in the Ohmic Polarization Region of Fuel Cells, *ACS Applied Materials & Interfaces* **2022**, *14*, 16108-16116
- [41] Z. Wang, J. Huang, L. Wang, Y. Liu, W. Liu, S. Zhao, Z.-Q. Liu, Cation-Tuning Induced d-Band Center Modulation on Co-Based Spinel Oxide for Oxygen Reduction/Evolution Reaction, *Angewandte Chemie International Edition* **2022**, *61*, e202114696
- [42] Y. Yuan, Z. Jiang, M. Li, K. Peng, Magnetic Field Enhancing the Electrocatalytic Oxygen Evolution Reaction of FeMn-Based Spinel Oxides, *ACS Applied Energy Materials* **2023**, *6*, 7865-7876
- [43] M. S. Matseke, H. Zheng, M. K. Mathe, E. Carleschi, B. Doyle, Influence of Co doping on physiochemical properties of MnFe<sub>2</sub>O<sub>4</sub>/C nano compounds toward oxygen reduction reaction, *Journal of Alloys and Compounds* **2021**, *888*, 161581
- [44] T. C. Kaspar, P. V. Sushko, S. R. Spurgeon, M. E. Bowden, D. J. Keavney, R. B. Comes, S. Saremi, L. Martin, S. A. Chambers, Electronic Structure and Band Alignment of LaMnO<sub>3</sub>/SrTiO<sub>3</sub> Polar/Nonpolar Heterojunctions, *Advanced Materials Interfaces* **2019**, *6*, 1801428
- [45] M. Abirami, S. M. Hwang, J. Yang, S. T. Senthilkumar, J. Kim, W.-S. Go, B. Senthilkumar, H.-K. Song, Y. Kim, A Metal–Organic Framework Derived Porous Cobalt Manganese Oxide Bifunctional Electrocatalyst for Hybrid Na–Air/Seawater Batteries, *ACS Applied Materials & Interfaces* **2016**, *8*, 32778-32787
- [46] P. W. Menezes, A. Indra, V. Gutkin, M. Driess, Boosting electrochemical water oxidation through replacement of Oh Co sites in cobalt oxide spinel with manganese, *Chemical Communications* **2017**, *53*, 8018-8021
- [47] X. Peng, F. Gao, J. Zhao, J. Li, J. Qu, H. Fan, Self-assembly of a graphene oxide/MnFe<sub>2</sub>O<sub>4</sub> motor by coupling shear force with capillarity for removal of toxic heavy metals, *Journal of Materials Chemistry A* **2018**, *6*, 20861-20868
- [48] I. Madakannu, I. Patil, B. Kakade, K. K. R. Datta, Electrocatalytic oxygen reduction activity of AgCoCu oxides on reduced graphene oxide in alkaline media, *Beilstein Journal of Nanotechnology* **2022**, *13*, 1020-1029
- [49] K. R. D. Kasibhatta, I. Madakannu, I. Prasanthi, Hetero Atom Doped Graphene Nanoarchitectonics as Electrocatalysts Towards the Oxygen Reduction and Evolution



Reactions in Acidic Medium, *Journal of Inorganic and Organometallic Polymers and Materials* **2021**, *31*, 1859-1876 View Article Online  
DOI: 10.1039/D6YA00052E

- [50] D. Navadeepthy, A. Rebekah, C. Viswanthan, N. Ponpandian, Boosting the kinetics of oxygen and hydrogen evolution in alkaline water splitting using nickel ferrite /N-graphene nanocomposite as a bifunctional electrocatalyst, *International Journal of Hydrogen Energy* **2021**, *46*, 21512-21524
- [51] A. Al Mahmud, M. R. Thalji, G. Dhakal, Y. Haldorai, W. K. Kim, J.-J. Shim, Bifunctional MoC/NiC@N-doped reduced graphene oxide nano electrocatalyst for simultaneous production of hydrogen and oxygen through efficient overall electrochemical water splitting, *Materials Today Nano* **2024**, *27*, 100489
- [52] X. Xing, R. Liu, K. Cao, U. Kaiser, G. Zhang, C. Streb, Manganese Vanadium Oxide–N-Doped Reduced Graphene Oxide Composites as Oxygen Reduction and Oxygen Evolution Electrocatalysts, *ACS Applied Materials & Interfaces* **2018**, *10*, 44511-44517
- [53] Y.-Z. Hu, S.-F. Zhang, X.-L. Han, Y. Liu, Recent progress in non-noble metal nano-electrocatalysts for hybrid water splitting, *Nanoscale* **2025**, *17*, 6362-6389
- [54] B. H. R. Suryanto, Y. Wang, R. K. Hocking, W. Adamson, C. Zhao, Overall electrochemical splitting of water at the heterogeneous interface of nickel and iron oxide, *Nature Communications* **2019**, *10*, 5599
- [55] X. Wang, X. Li, B. Li, W. Wang, S. Bai, S. Zai, Z. Ni, C. Meng, Surface-reconstructed FeOOH@CoFeOS/NF architectures: leveraging nano-layered stacking for accelerated oxygen evolution kinetics, *New Journal of Chemistry* **2025**, *49*, 1506-1512
- [56] J. Zhu, J. Qian, X. Peng, B. Xia, D. Gao, Etching-Induced Surface Reconstruction of NiMoO<sub>4</sub> for Oxygen Evolution Reaction, *Nano-Micro Letters* **2023**, *15*, 30
- [57] Z. Xiao, J. Wang, C. Liu, B. Wang, Q. Zhang, Z. Xu, M. T. Sarwar, A. Tang, H. Yang, In-situ surface structural reconstruction of NiMoO<sub>4</sub> for efficient overall water splitting, *Applied Surface Science* **2022**, *602*, 154314



View Article Online  
DOI: 10.1039/D6YA00052E

Open Access Article. Published on 22 April 2026. Downloaded on 4/22/2026 9:46:03 PM.  
This article is licensed under a Creative Commons Attribution-NonCommercial 3.0 Unported Licence.



## Data Availability Statement

View Article Online  
DOI: 10.1039/D6YA00052E

### The supporting data has been provided as part of the Supplementary information

Supporting information contains detailed materials and methods, physical and electrochemical characterization details, calculation methods, XRD of synthesised GO, FT-IR and spectra of  $\text{MMn}_2\text{O}_4$  oxides (M= Fe, Co, Cu and Zn) embedded over N-rGO, Survey scan and HR- XP spectra of C 1s of  $\text{FeMn}_2\text{O}_4@\text{N-rGO}$  heterostructures, HR -XP spectra of  $\text{CuMn}_2\text{O}_4@\text{N-rGO}$ ,  $\text{CoMn}_2\text{O}_4@\text{N-rGO}$  and  $\text{ZnMn}_2\text{O}_4@\text{N-rGO}$  heterostructures, LSV curves of N-rGO,  $\text{FeMn}_2\text{O}_4$ ,  $\text{FeMn}_2\text{O}_4@\text{rGO}$  and  $\text{FeMn}_2\text{O}_4@\text{N-rGO}$ . HER polarization curves and Tafel analysis of  $\text{MMn}_2\text{O}_4$  (M = Fe, Co, Cu, and Zn) oxides embedded on N-rGO, HR- XP spectra overlap of  $\text{MMn}_2\text{O}_4$  oxides (M= Fe, Co, Cu and Zn) embedded over N-rGO, Proposed OER mechanism, Water contact angle measurement, ECSA of  $\text{FeMn}_2\text{O}_4@\text{N-rGO}$  heterostructures, Isolated cathodic (reduction) peaks extracted from the CV curves of  $\text{MMn}_2\text{O}_4$  oxides (M= Fe, Co, Cu and Zn) embedded over N-rGO, HR-XPS after and before OER of the  $\text{FeMn}_2\text{O}_4@\text{N-rGO}$  heterostructures, Summary of OER activity metrics of prepared electrocatalyst, Comparative OER performance of  $\text{FeMn}_2\text{O}_4\text{-N-rGO}$  heterostructures with recently reported electrocatalysts.

